Title

Buried Aseismic Slip and Off-Fault Deformation on the Southernmost San Andreas Fault Triggered by the 2010 El Mayor Cucapah Earthquake Revealed by UAVSAR

Journal

Earth and Space Science, 8(8)

ISSN

2333-5084

Authors

Parker, Jay

Donnellan, Andrea

Bilham, Roger

et al.

Publication Date

2021-08-01

DOI

10.1029/2021ea001682

Earth and Space Science

RESEARCH ARTICLE
10.1029/2021EA001682

Special Section:
Results from 10 Years of UAVSAR Observations

Buried Aseismic Slip and Off-Fault Deformation on the Southernmost San Andreas Fault Triggered by the 2010 El Mayor Cucapah Earthquake Revealed by UAVSAR

Jay Parker[1], Andrea Donnellan[1], Roger Bilham[2], Lisa Grant Ludwig[3], Jun Wang[4], Marlon Pierce[4], Nicholas Mowery[5], and Susanne Jänecke[6]

[1]Jet Propulsion Laboratory, California Institute of Technology, Pasadena, CA, USA, [2]Geological Sciences and Cooperative Institute for Research in Environmental Sciences, University of Colorado, Boulder, CO, USA, [3]Program in Public Health, University of California, Irvine, Irvine, CA, USA, [4]Pervasive Technology Institute, Indiana University, Bloomington, IN, USA, [5]Applied Research Associates, Inc., Albuquerque, NM, USA, [6]Department of Geosciences, Utah State University, Logan, UT, USA

Abstract We use UAVSAR interferograms to characterize fault slip, triggered by the Mw 7.2 El Mayor-Cucapah earthquake on the 1 San Andreas Fault in the Coachella Valley providing comprehensive maps of short-term geodetic surface deformation that complement in situ measurements. Creepmeters and geological mapping of fault offsets on Durmid Hill recorded 4 and 8 mm of average triggered slip respectively on the fault, in contrast to radar views that reveal significant off-fault dextral deformation averaging 20 mm. Unlike slip in previous triggered slip events on the southernmost San Andreas fault, dextral shear in 2010 is not confined to transpressional hills in the Coachella valley. Edge detection and gradient estimation applied to the 50-m-sampled interferogram data identify the location (to 20 m) and local strike (to <4°) of secondary surface ruptures. Transverse curve fitting applied to these local detections provides local estimates of the radar-projected dextral slip and a parameter indicating the transverse width of the slip, which we equate with the depth of subsurface shear. These estimates are partially validated by fault-transverse interferogram profiles generated using the GeoGateway UAVSAR tool, and appear consistent for radar-projected slip greater than about 5 mm. An unexpected finding is that creep and triggered slip on the San Andreas fault terminate in the shallow subsurface below a surface shear zone that resists the simple expression of aseismic fault slip. We introduce the notion of a surface locking depth above which fault slip is manifest as distributed shear, and evaluate its depth as 6–27 m.

Plain Language Summary An aircraft-mounted imaging radar relies on a highly sensitive reflected interference pattern to form precise maps of surface changes. Images obtained from flights before and after the April 4, 2010 magnitude 7.2 El Mayor-Cucapah earthquake view the San Andreas Fault in California's Coachella Valley. Although the earthquake occurred 75 miles to the south of this fault, computer vision brings out complicated reshaping near and on the fault. The quiet deformation is concentrated in patches along the fault between the Mecca Hills and the Salton Sea, and matches the sense of slip expected from long-known continental plate motions surrounding this region. Slip at the fault surface are radar-measured at less than 3/4" but when compared to measurements in the broader fault zone we find that slip triggered by the distant earthquake is usually confined below a level 30 feet beneath the surface, reshaping a zone around the fault more than one hundred and 80 feet wide. This newly discovered barrier may be an interwoven network of clay lumps in the fault zone. Our finding explains why the process of slow fault slip is rarely obvious on the surface, but is usually observed as a series of discontinuous cracks following the fault.

Key Points:

- Airborne radar interferograms map displacement in the Coachella Valley using visits before and after the El Mayor Cucapah earthquake
- UAVSAR-determined triggered slip on southern San Andreas and Hidden Spring fault has distinct slip zones and gaps
- Concentrated deformation at the San Andreas Fault displays a variable-width deformation zone

Correspondence to:
J. Parker,
Jay.W.Parker@jpl.nasa.gov

Citation:
Parker, J., Donnellan, A., Bilham, R., Ludwig, L. G., Wang, J., Pierce, M., et al. (2021). Buried aseismic slip and off-fault deformation on the southernmost San Andreas fault triggered by the 2010 El Mayor Cucapah earthquake revealed by UAVSAR. *Earth and Space Science*, *8*, e2021EA001682. https://doi.org/10.1029/2021EA001682

Received 25 JAN 2021
Accepted 26 JUL 2021

1. Introduction

The Coachella Section of the San Andreas Fault (SAF) has accumulated considerable stress since its last major earthquake, c1700 CE (discussed below), and for the past few decades has exhibited surface creep amounting to 2–4 mm/yr. The southern SAF and major plate boundary features are displayed in Figure 1. This southernmost ~70 km segment of the SAF is the least-well understood part of the plate-boundary-defining ~1,100 km long SAF, with respect to hazard and the timing of the next large event (Philibosian

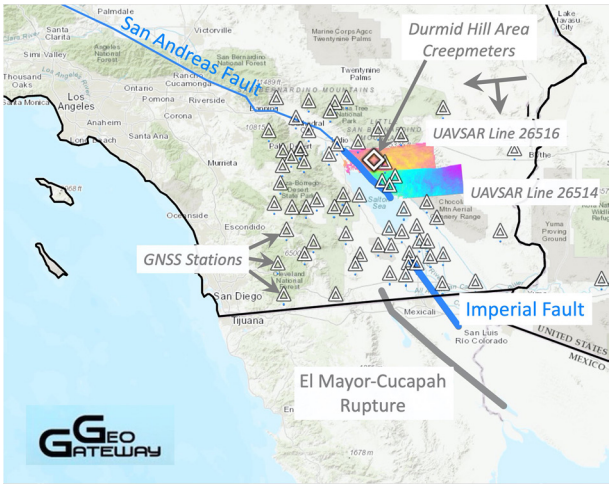

Figure 1. Southern San Andreas Fault, Imperial Fault (blue), and El Major Cucapah rupture (gray). Durmid Hill area creepmeters (locations in Figure 6), arrowed. GNSS stations = triangles. This scene is located at (Lon, Lat) −116.2, 33.7.

et al., 2011). Other than the Creeping Section in central California, it is the only portion that has not had an earthquake described in historical archives and its contribution to earthquake hazard have been entirely developed from paleoseismological data.

This southern section of the surface fault consists of six ≥12 km long segments. The fault is clearly expressed in transpressive hills where it strikes at N48 W, roughly 8° oblique to the local Pacific/North America slip vector, but is weakly expressed in intervening segments with similar length, low elevation and more northerly strike. Intriguingly, localized fault creep and triggered slip are almost exclusively confined to the Indio Hills, Mecca Hills and Durmid Hill segments of the fault (Bilham & Williams, 1985; Lindsey et al., 2014). Triggered creep on the southern SAF has been reported for nearby moderate to large earthquakes beginning with the 1,968 Mw 6.5 Borrego Mountain earthquake (Allen et al., 1972) and for numerous subsequent nearby earthquakes (Bilham & Castillo, 2020; Tymofyeyeva et al., 2019; Wei et al., 2011; Williams et al., 1988).

Paleoseismic trench investigations indicate a 300-year mean slip rate near Indio of 3.4 ± 0.7 mm, and 4 ± 1 mm near Ferrum (Sieh & Williams, 1990). Sieh (1986) estimates the most recent major rupture occurred in 1,680, whereas Rockwell et al. (2018) take into account effects of inundations and conclude that the Coachella Section ruptured in C.E. 1,726 ± 7 and 1,577 ± 67 (two sigma). In either case, the mean recurrence time was found to be ~180 years. Almost 300 years has elapsed since the most recent major earthquake, the longest interevent time recorded in these referenced studies. Geodetic and geologic fault rate estimates are ~20 mm/yr near this location, showing close agreement (Tong et al., 2014). Lundgren et al. (2009) use GNSS network velocities and ERS interferograms to derive a 17 mm/yr geodetic rate on the southern SAF. These estimates substantially agree with estimates of surface features. Van der Woerd et al. (2006) employ isotopic dating of an offset alluvial fan surface in the Indio Hills (about 30 km north of our study area), determining long-term slip of 15.9 +- 3.4 mm/yr, while Behr et al. (2010) derive a preferred estimate of ~14–17 mm/yr. Taken together, the slip deficit may be considered to be about 5–6 m, which indicates a potentially disastrous future event.

Two-pass interferometric synthetic aperture radar (InSAR) results in georeferenced maps of the temporal change in the returned phase, resulting from deformation of surface features mixed with imprints of changes to the propagation media and to surface electromagnetic constitutive properties. Decades of satellite InSAR observations of the southern SAF show evidence of a shallow horizontal average slip rate ranging from 2-5 mm/yr. Lyons and Sandwell (2003) examine southern SAF broad deformation and localized slip in ERS stacked interferograms, identifying up to 10 and 1 cm slip corresponding to the 1993 Landers and 1999 Hector Mine 1999 earthquakes, and 4–6 mm/yr diffuse deformation in the interseismic period. Fialko (2006) observes stacked interferograms between 1992 and 2000, finding accumulated strain partitioned between the SAF and SJF. They conclude the observed strain is consistent with high material contrast across each fault (3x higher sheer modulus on the west side of each, vs. the east sides), with a slip rate of 25 mm/yr and a locking depth of 17 km for the southern SAF, and 21 mm/yr and 12 km, respectively, for the San Jacinto fault. Manzo et al. (2012) use the SBAS DInSAR time series method to image Coachella Valley deformation in the 1992–2006 ERS-1/2 radar observations, showing consistent time series from the radar compared to local GNSS stations. Lindsey et al. (2014) show that for 2003–2010 Envisat images the localization of slip varies with the meandering strike of the fault trace, with high localization on transpressive segments and broad (up to 1.5 km wide) shear zones occurring in transtensive segments. Xu et al. (2018) examine 25 years of ERS, Envisat and Sentinel interferograms and detect rate changes on decadal scales, modulated by large earthquakes. They conclude static stress changes may cause this variation in shallow creep rates.

Wei et al. (2011) report triggered slip on the SAF slip accompanying the 2010 El Major Cucupah earthquake, and use ALOS ascending and ENVISAT descending data to distinguish vertical from horizontal displacement. SAF horizontal offsets are recorded as up to 32.3 ± 8.1 mm, and vertical offsets of −8.8 ± 3.8 mm

Table 1
UAVSAR Data Products, Dates

UAVSAR product name	Visit1	Visit2	PixelToRadarBearing
SanAnd_26516_09015-010_10028-007_0354d_s01_L090HH_01	24Apr2009	13Apr2010	355
SanAnd_26514_09015-001_10028-005_0354d_s01_L090HH_01	24Apr2009	13Apr2010	355

(That is, the southwest side moves up according to their Table 1; their text says the opposite). The extensive Rymer et al. (2010) field survey does not identify corresponding vertical slip on the Coachella Segment.

Rymer et al. (2010) describes field reconnaissance covering much of the Salton Trough region, documenting hand-measured EMC-triggered slip at two dozen locations on the SAF Coachella Section. They observe about 29 km of discontinuous surface breaks, in broad areas of the Mecca Hills and between North Shore and Salt Creek, and no slip in other portions of the SAF. These observations reveal up to 18 mm dextral slip (Mecca Hills) with no discernable dip-slip component. They also report for the first time the use of UAVSAR to identify surface offsets in the Yuha Desert near the California-Mexico border, that were used for field identification and quantification of fault offsets. Many of these faults were newly discovered from UAVSAR imagery. Their report states "The approach that proved most rewarding was to use interferograms prepared by NASA's Uninhabited Aerial Vehicle Synthetic Aperture Radar (UAVSAR) to map surface dislocations, then find these sites in the field for visual verification and fault-displacement measurements."

Hazard is not limited to the southern SAF, as there is recognized potential for a combined event with the San Bernardino segment and other regional faults. The 2008 hypothetical "Shake Out" scenario earthquake postulated a Mw 7.8 combined rupture from the Salton Sea to Lake Hughes in the San Gabriel Mountains, radiating disastrous levels of seismic energy into the Los Angeles Basin and spawning in rapid succession M7 aftershocks in the Imperial Valley and the Cucamonga Fault bordering the heavily populated San Gabriel Valley (Jones et al., 2008).

The current study focusses on slip triggered by the 2010 El Major Cucapah (EMC) Mw = 7.2 earthquake. It is part of a broader effort to address key questions regarding California seismic hazard, namely: Is the hazard as high as expected from a simple recurrence model? Are paleoseismic data representative of Coachella rupture history? What is the significance of creep in assessing rupture potential? How is slip, including aseismic creep, distributed spatially and temporally? What are the implications of slip distribution for inferring the rheology of the shallow crust in the Salton Trough and Coachella Valley? How is slip partitioned between seismic and aseismic processes, and between strands of the San Andreas system? Relevant observation types are increasing rapidly, so this is also an effort to determine the extent to which UAVSAR observations complement paleoseismology, as well as present-day in situ and remote sensing of this critical fault section in a practical way. Airborne radar interferometry provides broader coverage than field work with far less physical effort, but requires inference of some components of motion due to geometric limitations and sources of interference.

Creep is recorded on the southern San Andreas and Superstition Hills faults during the earthquake and by additional creepmeters installed after the earthquake on some of these newly identified faults (Rymer et al., 2010). Several continuous GNSS stations of the NSF EarthScope Plate Boundary Observatory in the vicinity of the southern SAF record time series breaks at the time of the EMC earthquake, quantifying displacement in the vicinity of surface creep on local faults.

In past work we have reported slip triggered in 2010 on the Imperial, Superstition Hills, and East Elmore Ranch faults, (Donnellan et al., 2014), painstakingly estimated by projected displacements from the UAVSAR interferogram recorded as unwrapped phase. Automatic detection and characterization of surface fracture has been reported (Parker et al., 2018) and estimation of fault slip at depth and fracture zone width is added in Donnellan et al. (2018) to track continuing slip on the Yuha fault and the Ocotillo extension of the Elsinore fault over a seven-year period using many interferograms.

Table 1 lists the UAVSAR products highlighted in this work. Line 08517 overlaps some of line 26516 and also shows evidence of intermittent slip seen from the conjugate direction (looking north), not presented

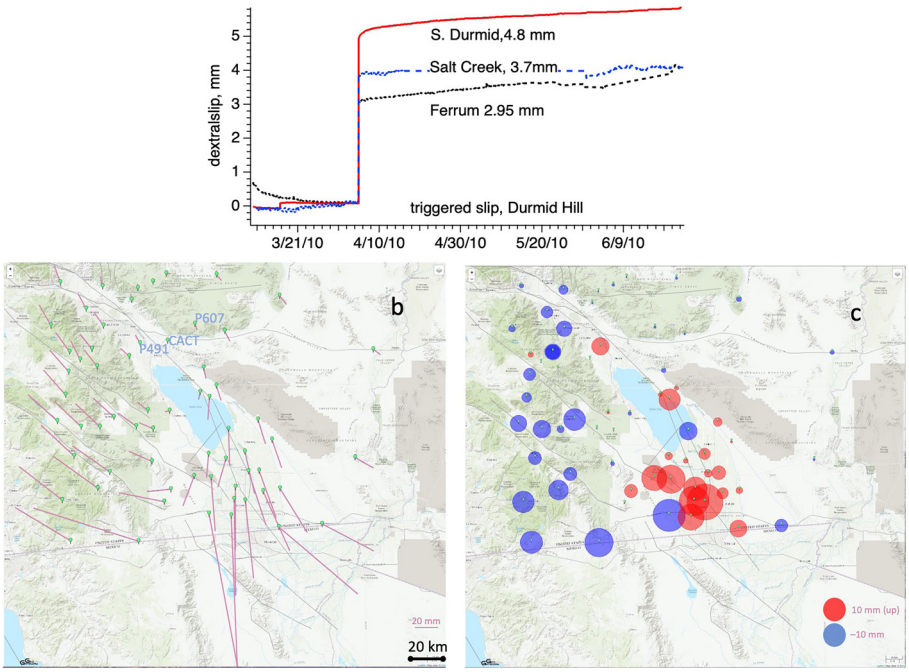

Figure 2. Creepmeter and GNSS products. (a) Creepmeters recorded extension (at 30° obliquity to the fault) ~3–5 mm between contiguous 5-min samples at three locations on Durmid Hill. Minor additional slip (<0.2 mm) occurred in the following few weeks. (b) & (c): GNSS station displacements corresponding to dates of UAVSAR visits 2009Apr24, 2010Apr13 bracketing the El Major Cucapah earthquake with fixed station CACT, east of the Coachella Valley. (b) Horizontal component indicates dextral shear imposed on southernmost San Andreas Fault. P491 and P607 record 14 mm dextral shear. (c) Vertical displacement. Red signifies upward motion, blue downward; largest red circle indicates 15 mm upward. Region to west of Coachella Valley is displaced downward ~10 mm, region to east shows little motion, while Salton Trough is displaced upward, particularly south of the Salton Sea (~15 mm).

here. Line 26518, parallel to 26516 and adjacent to the north, does not show evidence of EMC coseismic slip on the SAF.

In following sections, we summarize interferometry records of slip triggered by the El Major Cucapah earthquake. We infer this slip to have been induced by shaking accompanying the passage of surface waves from the earthquake. We then present mapped slip on the southern SAF as observed by UAVSAR repeat-pass unwrapped interferograms, including a detailed comparison of the automated characterization of subsurface slip and fault-zone width with many displacement profiles taken across the SAF in the Mecca Hills. Triggered slip is detected and estimated from a second UAVSAR interferogram, covering the receding shore of the northern Salton Sea.

1.1. Creepmeter and GNSS Measurements

The surface ruptures of the EMC earthquake are shown on Figure 1, together with the trace of the southern SAF and the Imperial Fault. The figure also shows the location of creepmeters (Bilham & Castillo, 2020), GNSS permanent stations, and the Table 1 UAVSAR data images spanning the date of the earthquake.

Creepmeter time series near the time of EMC and GNSS 3-d deformation between 24April2009 and 13April2010 (the dates of UAVSAR observations) are shown in Figure 2. GNSS displacements for the time period between the radar visit dates are displayed in Figures 2b and 2c using the GeoGateway GNSS tool (Heflin et al., 2020). The horizontal GNSS vectors indicate a pattern of coseismic dextral displacement across the Coachella Section of the SAF, and also a pattern of relative vertical motion across the Coachella Valley, downward on the west side, and a strong pattern of coseismic uplift in the entire Salton Trough, particularly at the south end.

Table 2
Relative Motion Between GNSS Stations P471, P607, With Formal Errors

Station	Timespan	DeltaE (mm)	DeltaN (mm)	Amplitude (mm)	Comment
P491	Coseismic: 04Apr2010	-0.04 ± 0.8	-14.5 ± 1.0	15	Estimated break
P607	Coseismic: 04Apr2010	1.1 ± 0.8	-14.6 ± 0.9	15	Estimated Break
P607–P491	Coseismic: 06Apr2010-02Apr2010	1.1 ± 1.2	-0.0 ± 1.4	1.1	From model fit to time series
P607–P491	RadarVisits: 24Apr2009-13Apr2010	8.7 ± 0.4	-10.7 ± 0.5	13.8	Using 10-day mean positions (Figure 2)
P607–P491	Velocity > 15 years	8.5 ± 0.2	-11.0 ± 0.2	13.9	Annualized over station lifetime, excluding breaks

GNSS relative motion between the sites P491 and P607 for significant time spans are listed in Table 2. These two sites (Coachella Valley and NE of Mecca Hills), span the area of interest. While both stations move about 14.5 mm to the south within a day of the earthquake, coseismic relative dextral displacement across the southernmost San Andreas fault is insignificant (1.1 ± 1.2 mm). Table 2 shows relative motion between the two sites spanning the radar visits (Figure 2b) is indifferent from interseismic velocities. The displacement arrows in the northern part of the figure similarly reflect 354 days of interseismic motion, while the displacements in the southern part are dominated by coseismic motion.

Seismicity in the radar visit time span has been investigated with the GeoGateway Seismicity Tool (Donnellan et al., 2021), which uses the USGS catalog service at https://earthquake.usgs.gov/earthquakes/map/. There are no catalog earthquakes > Mw 2.5 within 10 km of the SAF within the area covered by radar lines 26516 and 26514.

2. Surface Fracture Characterization by Image Analysis

UAVSAR unwrapped repeat-pass interferograms (RPI) indicate the radar line-of-sight (LOS) component of relative displacements across the image. Each sample corresponds to a 6 m pixel footprint at mid-latitudes. Consecutive images on a repeating linear flight path reveal changes to the landscape between the dates of the radar flights. For the formation of interferometric fringes, the first flight path must be repeated by succeeding flights to within a distance of 5 m (Hensley et al., 2009). This is made possible by a custom autopilot system guided by GPS real time positioning on-board the aircraft (Hensley et al., 2008). This NASA UAVSAR system has unique capabilities compared to satellite InSAR systems: flight lines may be arbitrarily configured to provide near-optimal measurements of crustal processes, including earthquakes and triggered slip associated with active surface tectonics. Ionospheric interference is avoided by flying at stratospheric altitudes, a comparatively low vantage point that allows high resolution imagery. Noise in the UAVSAR system is chiefly from unmodeled atmospheric refraction and residual errors in flight path positioning. These effects are characterized by broad (>km-scale) variations in recorded phase, and so are essentially negligible in the estimation of shear near a fault. Differential phase noise at high spatial frequency appears to be dominated by speckle noise, which is reduced but not fully eliminated by filtering (moving boxcar averaging) followed by downsampling.

In past work we have developed image analysis using the Canny computer vision method (Canny, 1986) for edge detection to determine candidate pixels for characterizing surface fractures. We employ the *Python OpenCV* module for this. Initial development and results characterizing triggered fault slip are described in Parker et al. (2018). That work documents automatic estimates of slip induced by the El Major earthquake on minor faults in the Yuha Desert of California, detection of postseismic slip on the Yuha fault and detection of a previously unknown transition fault connecting the Laguna Salada fault with the Elsinore fault. It also reports on the initial detection of coseismic slip on the southern SAF (in line 26514) and estimates coseismic and triggered slip in the 2014 M6.0 South Napa earthquake. A refinement of the method and its application to the estimation of seven years of afterslip on the Yuha Fault and the Laguna Salada-Elsinore transition fault are reported in Donnellan et al. (2018).

Table 3
Image Processing Stages Generating Edge Detection/Surface Fracture Maps and Tables

Stage 1	Read LOS radar displacements from unwrapped ground-range UAVSAR file.
Stage 2	Prepare image: determine missing or rejected pixels, fill with smooth values.
Stage 3	Use global *Canny* algorithm to find list of edge-bearing cells, candidates for surface slip.
Stage 4	Examine environment of each edge cell: evaluate along-gradient samples, and generate KMZ map of sense of slip.
Stage 5	Iteratively find width and amplitude: create table, KMZ partially transparent image.

Phase edges in radar-coherent regions identify locally concentrated displacement gradients, which we tentatively interpret as slip on a shallow or surface dislocation when they coincide with a mapped surface fault, particularly when the sense of the phase gradient agrees with the reported rake of the fault, as is the case for the HSF and SAF segments reported below. The sense of the surface displacement is not directly determined by a single interferogram, where the radar view is from a single direction. Displacement may be horizontal as with strike-slip fault creep, or partly vertical as with dip-slip faults or differential subsidence, or tensile, as with ridge spreading and some bedding plane shifts. In rare cases a phase edge is not caused by locally concentrated surface displacement gradient, such as occurs at a boundary between regions with a surface dielectric contrast, usually associated with surface moisture variations near aquicludes or local sources of irrigation.

The current method explores analysis of UAVSAR RPI phase-displacement images in five stages, listed in Table 3. Key stages are illustrated in Figure 3. These stages are uniformly applied in this work with parameters shown in Table 4. Note that in the current analysis we do not perform a least squares fit of the profile data to a parameterized arctan; rather, we employ a restriction of the profile to an area bounded by an inflection slope ratio profile (a measure of the concentration of the gradient and determination of where the profile flattens out), that effectively parameterizes the width and amplitude of the profile. The sometimes small number of accepted profile points sampled on a fixed grid contributes substantially to the local scattering of width estimates, but the estimate of the shear amplitude is robust, little affected by the filtering and the fixed grid.

The cell size in the UAVSAR unwrapped interferogram product corresponds to 5 m (east-west) × 6 m (north-south). At this sampling the profiles often show coseismic surface fault slip (e.g., portions of the South Napa rupture) resolved across three adjacent profile samples: the fault-crossing sample has an intermediate value, while the expected step function is otherwise fully reproduced. Resampling with 6 × 6 original cells results in 30 × 36 m cells, part of a spatial filtering method that renders improved continuity of fault traces at the expense of biasing upwards estimates of the shear zone width. As an example of the width bias, we performed a simulation of a 0-width fault in a half space, emulating radar phase on a 30 × 36 m sample grid. When subjected to the spatial filtering, edge detection and local width estimation used in this paper, shear-zone width estimates ranged from 8 to 30 m, with a mean value of 25 m.

Analysis in this section reports the radar LOS component of slip, s_R: the radar is sensitive to the component of displacement aligned with the line of sight from the ground patch to the aircraft. Because the aircraft views the ground from a known elevation angle e and azimuth, and the azimuth is misaligned with the fault strike by Δa, pure dextral slip s_D will be viewed as $s_R = s_D \cos(e)\cos(\Delta a)$. In Figures 3–7 the plotted slip is s_R, while inferred dextral slip s_D is reserved for the Discussion and Figure 8. Residual speckle noise appears to limit edge detection reliability below a threshold of about 5 mm, using the methods described below, and creates location-dependent uncertainty in the slip estimates that is difficult to characterize rigorously, but based on local scatter of estimates can range from 3–8 mm (3 sigma).

2.1. Slip on UAVSAR Line 26516 Near Mecca, California

Figure 4 shows the sense of slip in line 26516, and the final slip amplitude map. The sense of slip is analogous to the classic test of strike-slip fault motion, adapted for the radar viewpoint. The radar views the surface at an oblique angle, looking left referenced to its flight path. Flight line geometry and the sign of the

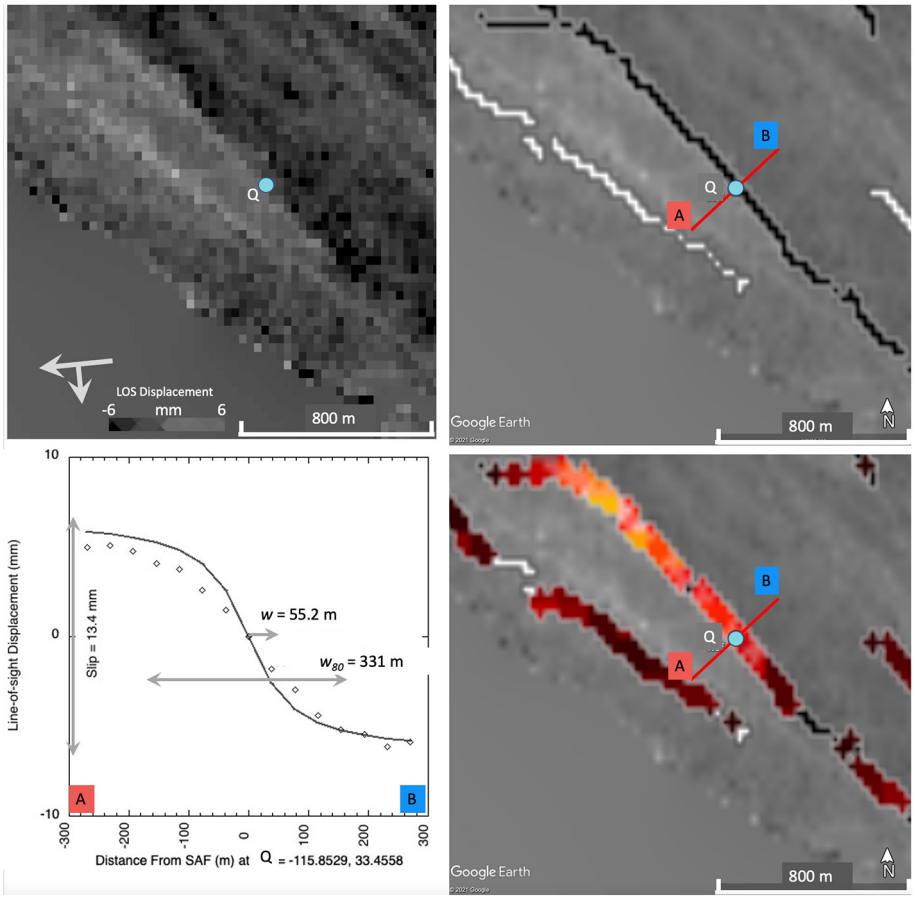

Figure 3. Illustration of edge-detection process and the subsequent derivation of slip and width. (a): Image preparation produces high-contrast grayscale image near North Shore, indicating Q point −115.8529, 33.4558 on the San Andreas Fault near North Shore. Rectangular pixels represent the 5 × 5 downsampled line-of-sight (LOS) displacement data from UAVSAR product file SanAnd_26514_09015-001_10028-005_0354d_s01_L090HH_01. unw. grd The flight direction (bearing 265) and left-looking radar line of sight are indicated with white arrows. The scene boundary is indicated in Figure 6a. (b) Same background image as viewed in Google Earth, with Canny-determined edges. Determined edge pixels are colored black corresponding to dextral slip and white for sinistral slip. Segment A-B is examined for zone width and slip. (c): Definition of LOS slip and width quantified for each detected local shear feature. Shown are the smoothed data values of LOS displacement, and the parameterized arctan function determined by data points retained by a bending criterion. Radar phase profile: diamonds; arctan fit: solid line. (d): Radar-viewed slip amplitude: Localized slip is color-coded according to slip amplitude (scale indicated in Figure 4).

phase gradient at detected edges are used to determine the sense of slip. As the radar views the environment of a detected edge, there must be relative displacement between the two sides adjacent to the edge. If the right side in the radar view is moving toward the radar, the edge is colored black, consistent with right lateral motion across a surface fracture. If the left side is moving relatively toward the radar, the edge is colored white, consistent with left-lateral motion. For the single-view images shown here, the radar cannot distinguish strike-slip from dip-slip motion. For edges corresponding to pure strike-slip motion, the black-white coloration of edges is a reliable indicator of the sense of that strike-slip motion, right or left lateral. Note in Figure 4a that nearly all detections on the SAF are colored black, indicating the triggered slip (when purely strike slip) is consistent with dextral motion.

A significant left stepover of the surface deformation occurs at the mouth of Painted Canyon in the Mecca Hills. A part of the Skeleton Canyon fault zone was activated by creep here and there along a zone that is up to 2 km long and located about 200 m NE of the main trace of the SAF, as Lindsey et al. (2014) also noted. An oblique white crossing edge appears to mark the edge of the Painted Canyon alluvial fan. Also note near North Shore, at the south-east end of this SAF segment there is indication of multistranded triggered slip.

Table 4
Image Processing Parameters

Rejection threshold, mean coherence *(Stage 2)*	<0.3 over 18 × 18 cells
Rejection threshold, displacement standard deviation *(Stage 2)*	<7 mm over 18 × 18 cells
Pre-canny smoothing kernel *(Stage 2)*	18 cells
Coherent down sampling *(Stage 2)*	6 × 6 cells
Canny aperture size *(Stage 3)*	5 down-sampled cells
Canny threshold *(Stage 3)*	5 mm
Canny hysteresis ratio *(Stage 3)*	0.75
Along-strike averaging *(Stage 5)*	None
Local inflection slope ratio threshold *(Stage 5)*	0.2
Slip KMZ image color lower saturation point *(Stage 5)*	5 mm
Slip KMZ image color upper saturation point *(Stage 5)*	20 mm

Detected edges to the southwest of the SAF are chiefly associated with man-made structures and agricultural field edges, while detected edges to the northeast occur in extremely rugged terrain, and may correspond to few-cm landslides, ridge spreading, bedding-plane slip or differential settling. Contorted and folded beds on Durmid Hill showing evidence of recent surface disturbance are mapped by Jänecke et al. (2018). Similarly, disturbed bedding planes are probably observed by UAVSAR in a subsidiary damage zone from the M5.2 La Habra earthquake (Donnellan et al., 2015). In the following we ignore features more than 500m from the SAF, to focus on triggered slip and associated off-fault deformation.

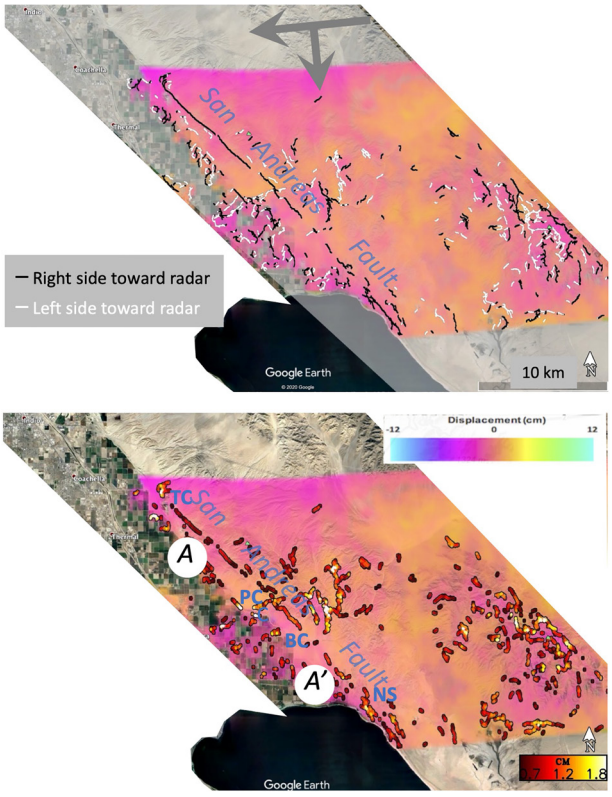

Figure 4. Segment of line 26516 coseismic interferogram crossing the San Andreas Fault (SAF). (a): Polarity of slip, black dextral, white sinistral. Data are quantified within 20-km-wide swath parallel to SAF. (b): Radar-observed amplitude of slip on localized shear zones coded according to 5–20 mm scale at lower right. Mapped fault shows as discontinuous throughgoing line between TC (Thermal Canyon) and NS (North Shore). PC: Painted Canyon, BC: Box Canyon. Portion from *A* to *A'* is detailed in Figure 5.

Figure 5 shows a 14-km selected segment of the SAF through the Mecca Hills, part of UAVSAR line 26516. The selection focuses on an area of intermittent slip, illustrating off-fault displacement for surface breaks, gaps, and shear zones. The panels represent the resolved components of width and slip for features identified in Figure 4b within about 500 m of the mapped fault trace (a limit chosen to minimize interference from man-made disturbances such as agricultural development). Continuous series are plotted at 500-m intervals orthogonal to the fault generated from the line 26516 interferogram data using the UAVSAR LOS profile tool of the GeoGateway application (geo-gateway.org). The width is parameterized as though the sigmoid were proportional to arctan (x/w) where x is the fault transverse distance. Note that estimated slip is the relative projected displacement across the entire detected shearing zone (Figure 3c), whether that resembles a step function or a sigmoidal curve. The arctan function (characteristic of buried elastic faulted slip) has a rather slow asymptotic approach to the region of full slip, so this reported width will typically be smaller than a visual estimate of the shear zone width. Evaluation of the arctangent function shows that 80% of the total shear displacement is contained within a band of width $w_{80} = 6w$, where w can be shown to represent the approximate depth to the top of subsurface dislocation in an elastic half-space (Savage & Prescott, 1978).

The information explicit in aligned panels of Figure 5 facilitate a partial validation of our automated estimates of slip and width. In the third panel the two left-hand profiles appear noisy, and correspond to spatially interrupted detection of the slip depicted in Figure 4. The next four profiles (when allowance is made for the spatial smoothing involved in forming the profile) show discrete localized offsets, symptomatic of slip

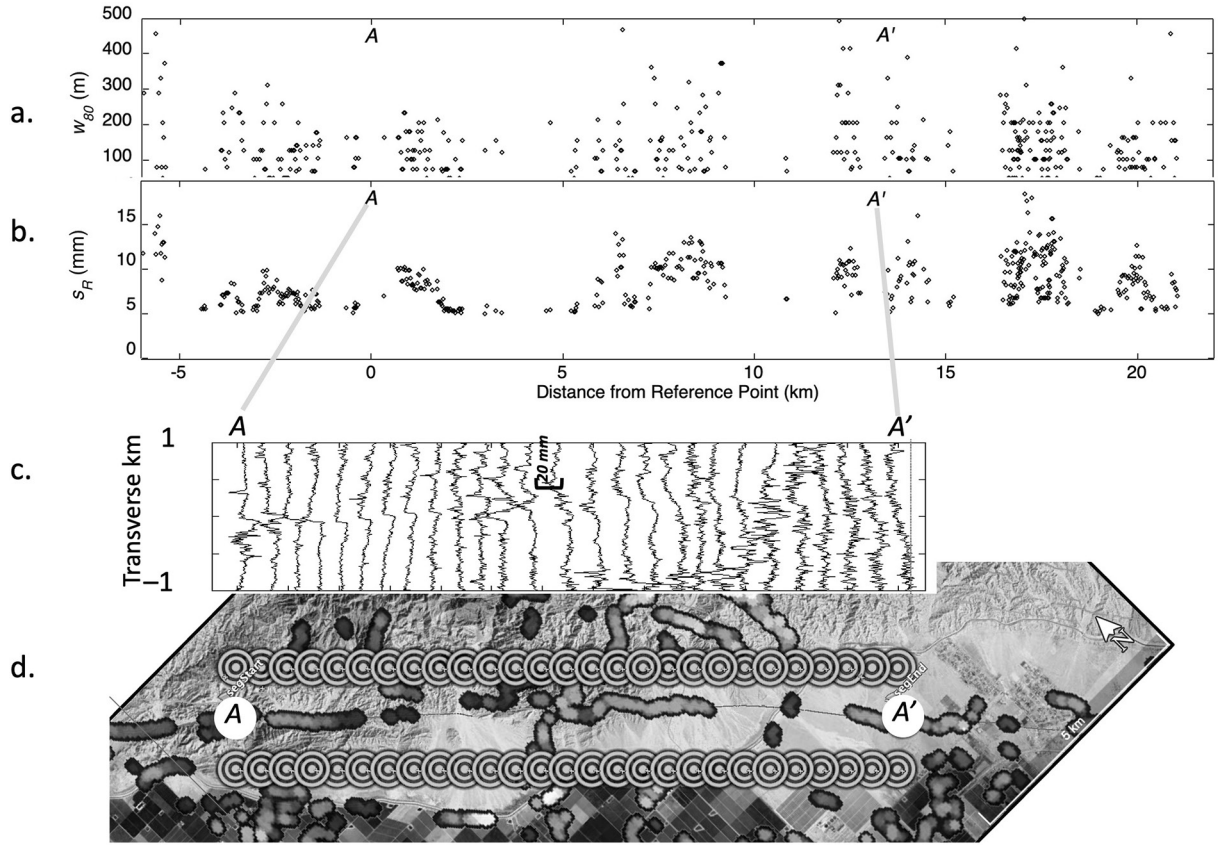

Figure 5. Mecca Hills segment of San Andreas Fault. (a) Width parameter w and (b) radar view slip s_{ir} for edges detected within 1 km of mapped fault. (c) 2-km-long line-of-sight (LOS) displacement profiles normal to fault extracted using GeoGateway UAVSAR LOS tool. Positive displacements imply ground position change toward the aircraft. Each 500 m spaced profile is the average of three contiguous profiles spaced at 50 m intervals. (d) Google Earth map view indicating start and end points of profiles in (c). Reference point is the on-fault target at 116.057539°W, 33.633535°N.

indistinguishable from rupture of a surface fault. The next three profiles show smaller jumps, close to the threshold of the image analysis and corresponding to intermittent slip markers on Figure 4. Profiles near the middle clearly indicate a broader shear zone, consistent with the larger width estimate cluster and also the larger slip values: the slip estimate embraces the total amplitude of the sigmoid characterizing the shear zone. A few points show detected slip from about 10–12.5 km from the start (the northwest most considered profile), corresponding to the noisy profiles that show no obvious trend. The last two profiles show a restoration of a broad trend, corresponding to the final cluster of ~10 cm slip across a ~50m width. These broader zones of deformation found at the end of the segment correspond to the distributed shear between transpressional segments described by Lindsey et al., 2014).

2.2. Slip on UAVSAR Line 26514, Northeast Flank of Salton Sea

Figure 6 shows the sense of slip, area of consideration, and slip magnitude estimates for line 26514, similar to Figure 4. This map is more complex, as we find in addition to SAF slip several other features highlighted by edge detection. The first right-lateral lineation NE of the SAF marks the Hidden Spring fault. Mixed-sense parallel lineations just east of the SAF farther south correspond to edges of a dry wash, that may have experienced coseismic settling. Other connected strands are associated with sloping sides of irrigation canals and hydrologic structures associated with this network of canals.

Figure 7 shows the width parameter w and radar-view slip s_R for points in Figure 6c selected to lie within about 500 m of the SAF trace. Note there are several consistently slipping sections, interrupted by gaps at reference point distances 2–3, 6–7, and smaller gaps at 11 and 14 km.

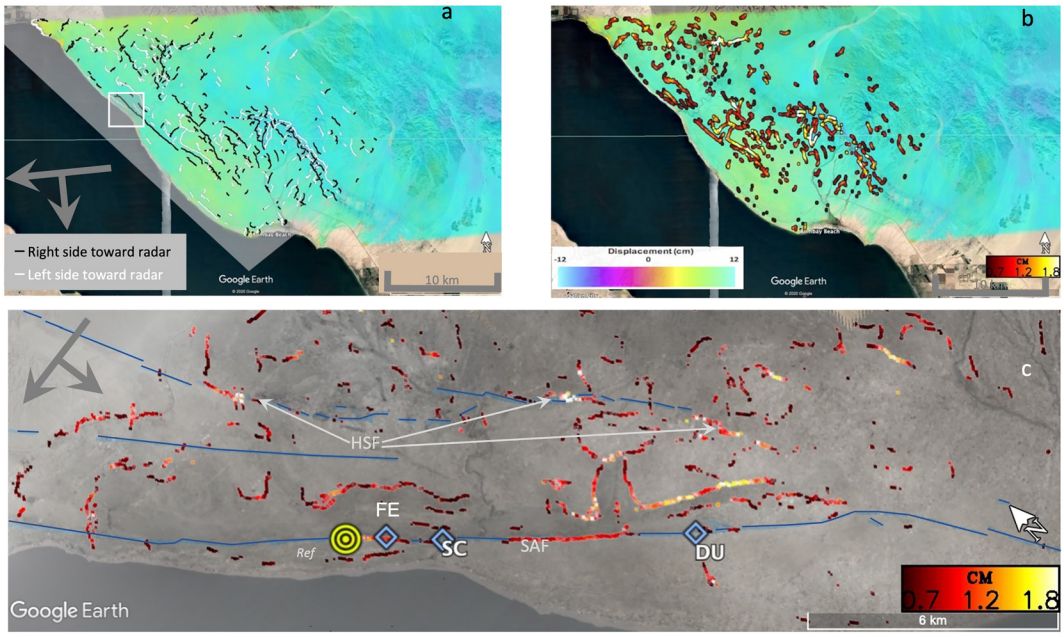

Figure 6. Durmid Hill segment of southern San Andreas Fault (26516 coseismic interferogram). (a): polarity and location of detected edges, black dextral, white sinistral. Boundary of Figure 3a is indicated by white square. (b): slip amplitude relative to radar line-of-sight. (c): Fault parallel view, of grayscale interferogram and heat-colored slip amplitudes (scale lower right), with fault traces from Quaternary Fault and Fold Database of the United States, blue (U.S. Geological Survey, 2020). Figure 7 is plotted relative to *Ref* (yellow). Creepmeters FE: Ferrum, SC: Salt Creek, DU: Durmid Hill. HSF: Hidden Spring Fault, SAF: San Andreas Fault.

3. Discussion

3.1. Detected Edges Frequently Correspond to Mapped Features

Most of the edges detected in this study can be associated with active faults, diverse geomorphic features, or shallow subsurface moisture gradients parallel to canals or paved highways (Figure 8). Localized phase gradients are centered on active right-lateral faults: the mapped surface strand of the San Andreas, Hot Springs and Powerline faults, and the western continuation of the Salton Creek fault zone. Some geomorphic features are also highlighted by detected edges: the high ridgelines of the Orocopia Mountains, the edges of large spits composed of lose sand and gravel deposited by Lake Cahuilla northeast of the main SAF,

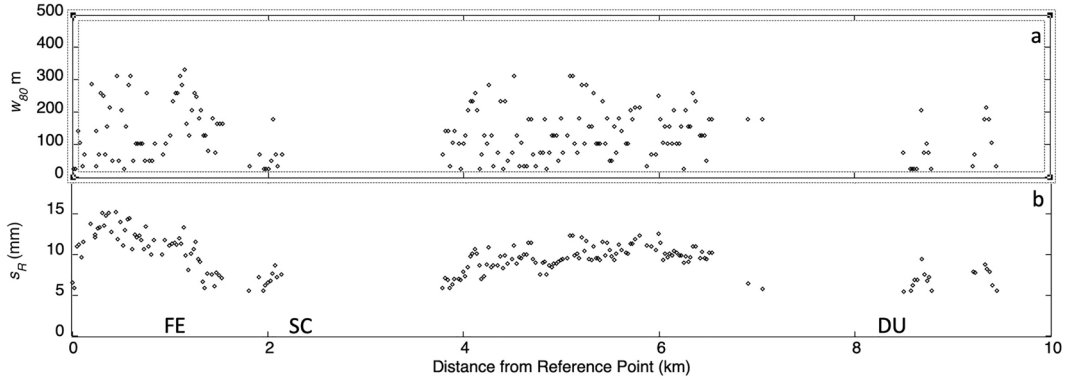

Figure 7. Line 26514 arctangent parameter fault motion estimates along the Durmid Hill segment, southern San Andreas Fault (SAF), versus km (SE) from point *Ref* at 115.86194°W, 33.462845°N (yellow target icon in Figure 6c). Fault parameters as determined according to Figure 3, and same as Figures 5a and 5b (a) Shear zone width parameter w_{80}. (b) Radar view of shear (slip) s_R on SAF. Radar view slip below 5 mm is not quantified. Creepmeters indicated FE, SC and DU.

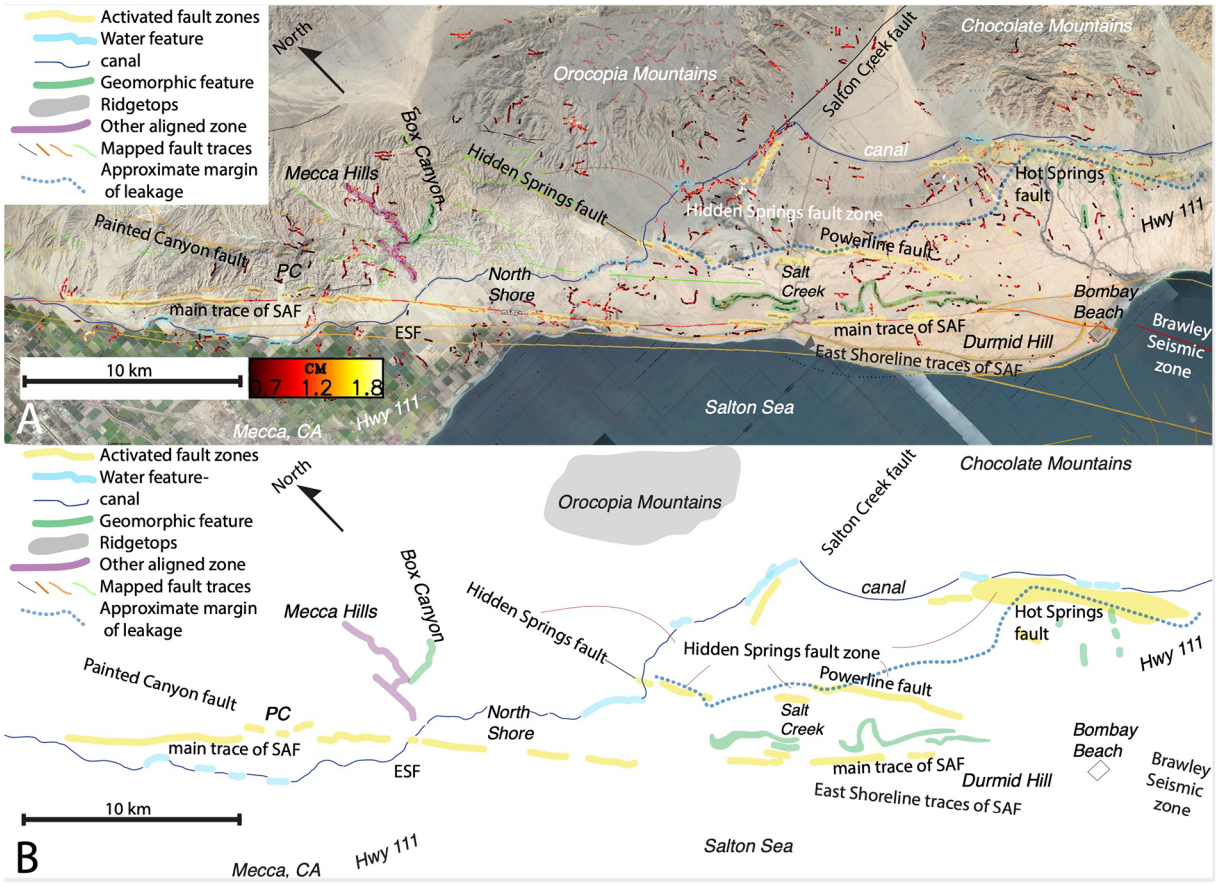

Figure 8. Correlation of detected edges with some mapped geologic and culture features, and additional features with no associated phase edges. (a) Composite annotated map including edges from Figures 4 and 6b, with line-of-sight edge amplitude shown in heat scale (range 5–20 mm). Hidden Spring fault zone is a ladder-like voluminous fault zone, similar to the southern San Andreas fault zone that has many small left-lateral cross faults and fewer master right lateral faults along its margins (Riemann et al., 2020). None of its internal cross faults showed evidence of creep. Fault traces are modified from Bryant (2012, 2015). (b) Selected mapped features in A, repeated without phase edges for clarity. Note the absence of creep along the main trace of San Andreas Fault along the southern 8 km of the fault and along other active faults. The "Approximate margin of leakage" refers to the position of the edge of displacement that we identified using 5 interferograms of Xu et al. (2018) below the Coachella canal and the vertical data set of Lindsey et al. (2014). In detail the boundary is more irregular than shown and it differs on each interferogram. ESF = East Shoreline fault of San Andreas fault zone. PC = Painted Canyon.

and the margins of channel fills in alluvium. Ridgetops in the Orocopia Mountains revealed concentrated phase gradients that might be precursors to deep-seated gravitational slope deformation (sackungen). There is also a notable correlation between concentrated phase gradients and areas of high hydrologic gradients: along the All American Canal, in the landscape downslope of the canal or adjacent to highway 111. A small fraction of the edges (10%–20%) do not correlate with any known phenomenon.

Fault segments of the Hidden Spring Fault show clear signs of concentrated phase gradients, which are often indicative of triggered fault slip. However, these segments are also down-slope from the Coachella Canal, a feature that invites interpretation in terms of fault zone permeability barriers. Although we cannot rule out some hydrologic impacts, we favor a tectonic interpretation of some or most of the phase gradients along the Hidden Springs and Powerline fault traces. Generally the phase gradients detected in the UAVSAR datasets and depicted in Figure 6 suggest that some short patches of the left-stepping Hidden Spring, Powerline and Hot Springs faults in the Hidden Spring fault zone may have experienced triggered slip or creep (Figure 8). We depict a simplified boundary of the zone of hydrologic deformation in Figure 8, based on Xu et al. (2018) and Lindsey et al. (2014). This facilitates comparison with mapped active faults. We note that while the first two segments are classified as Quaternary, and the latter Holocene (Jennings & Bryant, 2010) and there is no recorded dated earthquakes on these faults (neither historic or paleoseismic

events), triggered slip should not be ruled out in the light of reported accumulation of slip at high rates (either 5 or 12 mm/yr; Evans et al., 2015, 2016; see also Platt, 2017).

Consider first the Hot Springs segment at the southeastern end of the Hidden Spring Fault Zone. The Hot Springs fault zone generally coincides with the downslope margin of groundwater-related deformation in interferograms, it appears to localize the hydrologic effects of the leaking canal upslope of its linear trace, 1–2 km below the canal, in agreement with careful work of Bryant (1987). The impermeable nature of the Hot Springs fault zone limits our ability to separate tectonic effects from hydrologic effects along its trace.

The concentration of phase gradients detected along the Powerline fault, farther north (Figures 6 and 8), however, are likely to be entirely or mostly tectonic. The Powerline fault zone strikes 35° clockwise of the downslope margin of the hydrologic deformation imaged by Xu et al. (2018) and Lindsey et al. (2014) (Figure 8). The concentration of the phase gradients that we highlight in Figures 6 and 8 coincides with mapped traces of the Powerline fault zone while cutting obliquely through the edges of the downslope margin of the hydrologic deformation below the Coachella canal. The concentration of the phase gradients along the Powerline fault is mostly outside the influence of the formerly leaking canal (Figure 8).

The next fault zone farther north, the main trace of the Hidden Springs fault itself, has a strike ~80° to the local trend of the Coachella canal, and its concentration of phase gradients persists a few hundred meters above the canal (Figures 6 and 8). Xu et al. (2018) show that differential line of sight velocities across it continued even farther, up to 1.5 km north of the Coachella Canal in one of their interferograms that capture the El Mayor earthquake (their Figure 2). This pattern rules out hydrologic factors for the north end of the concentration of the phase gradients along the Hidden Springs fault. The high angle orientation of the Hidden Springs fault to the source of canal water and at an angle to gravity driven fluid flow, reduces the role of water and local impermeability on the concentration of the phase gradients in Figures 6 and 8.

The longest, most continuous edges follow the main trace of the SAF: three segments in the Mecca Hills (~7 km in NW Mecca Hills plus 3 km near Box Canyon), a handful of short segments near North Shore (~4 km total), and a <2.5 km segment northwest of Salt Creek and a 3.3 km segment to its southeast. Notably, the southernmost 9 km of the main trace of the SAF has little evidence for creep along it during this time period, whereas field observations since 2015 document numerous hairline fractures and eroding fractures along that part of the fault zone (Thomann et al., 2019). The East Shoreline strand of the SAF (Jänecke et al., 2018) lacks the strong signal of creep that characterizes most of the main traces of the SAF, and its wide deforming zone coincides mostly with short and inconclusive intervals of detected edges.

Altogether we detected creep along almost 20 km of the main SAF, from the highpoint of Durmid Hill northwestward through the Mecca Hills (Figure 8). This creep occurred in both more northwest-striking contractional and more northerly striking neutral parts of the SAF, as defined by Bilham and Williams (1985). Creep triggered by the 1968 Borrego Mountain earthquake, the 1979 Imperial Valley earthquake (Bilham & Williams, 1985) did not activate the North Shore segment of the SAF, and InSAR interferograms of the EMC earthquake (Lindsey et al., 2014) showed creep dispersed across a wider fault zone in the North Shore segment. In contrast, our UAVSAR-based datasets identify creep along short pieces of the main trace of the SAF within the North Shore segment (1.8 km or less) with displacements that are comparable to creep along the main SAF in the Mecca Hills and northwest of Durmid Hill. Creep was focused along shorter sections of the fault zone in the North Shore section and tended to activate longer sections in the Mecca Hills and near Salt Creek.

Some of the phase gradients with lateral extent can be equated with the edges and base of two large lacustrine spits that formed in shallow nearshore settings under Lake Cahuilla Sylvester et al., 1993). Two spit complexes are perches above a narrow horst of Mio-Pliocene Shavers Wells Formation, northeast of the San Andreas fault, near the Salton Sea. Both spit complexes coincide with detected edges along their northeast margin while somewhat less intense phase gradients occurred along their Aest margin (green lines in Figure 8). The base and edges of this large mass of unconsolidated sand and minor gravel forms a prominent signal in the data set. Altogether about 17 km of the contact between sand in the upper Holocene spit and underlying Pleistocene sedimentary rocks had noticeable displacement. This contact between sand and consolidated sedimentary rocks produced some of the largest displacements along 0.5- to 2 km-long

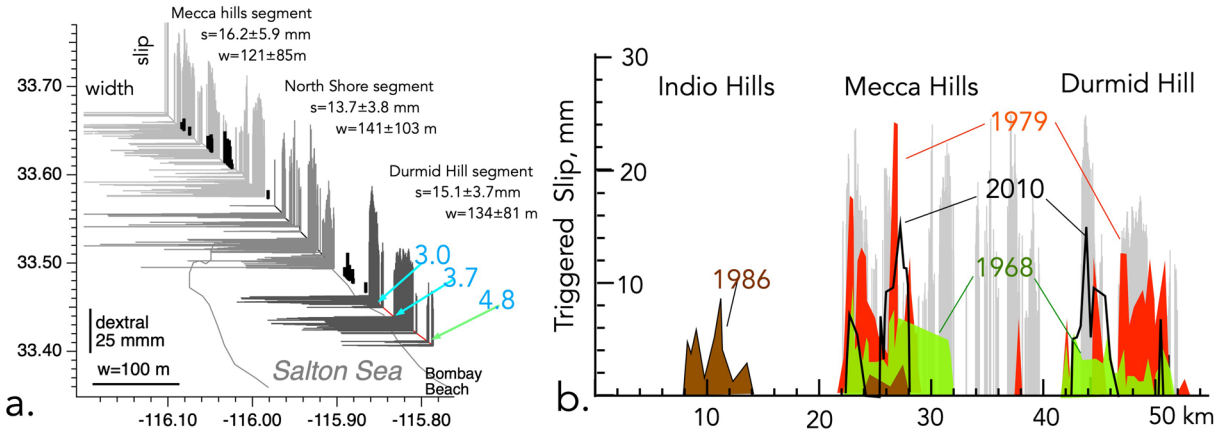

Figure 9. Radar observations compared with field measurements. (a) Radar observations of dextral slip and surface shear-zone width compared with field measurements of 2010 triggered slip (small black bars). Numerical averages for three identified segments of the fault are listed in the figure. Blue numbers indicate slip (in mm) recorded by creepmeters. (b) Mapped triggered slip in the 2010 earthquake (black line) is less extensive and numerically averages half that calculated from UAVSAR imagery (gray), and suggests that previous triggered slip (Williams et al., 1988) associated with earthquakes in 1968 (green), 1979 (red), and 1986 (brown) has been underestimated.

sections of the contact. 6 km of the edge produced a sinuous displacement boundary north of Salt Creek and a larger 7.2 km long NE margin and ~ 4.4 km Sw edge.

Three long and complex, multistranded bands of phase edges in the south-central Mecca Hills emanate north and south from Box Canyon and superficially appear to cross mapped faults of the Mecca Hills fault set (Hays, 1957; McNabb et al., 2017). Detailed examination of aerial photography shows, however, that there are disturbed beds and landscapes parallel to many NE, NNE, N and NW trending subsections of the two northerly trending strain bands. We predict that unmapped faults with small displacements are present and that these could have been triggered in this zone.

Our numerical estimates for localized off-fault slip and width indicate significant variation. Even on well-known faults, slip is discontinuous and separated by km-scale gaps. The scatter is partly inevitable as we are working close to the noise-level of our observing method. We do not quantify radar-view slip less than 5 mm. Comparisons with field measurements of triggered surface elsewhere (Parker et al., 2018) suggest that estimation error for radar-view slip s_R in moderate terrain with little vegetation is of the order of 8 mm, while in some heavily vegetated settings such as the Napa Valley, the bias plus random error is closer to 40 mm. The updated method used here appears to have random error ~0.3 mm based on sample variance for a 1 km subsegment (1.2–2.2 km from reference point) in segment 1 in Figure 5.

The shear displacements s_R in Figures 5 and 7b integrate shear to a distance of at least w_{80}, exploring a fault-centered band until sufficient samples are included to estimate arctangent profile, parameterized as slip and width. Hence over 80% of the estimated slip is directly measured in terms of radar LOS displacement, and the remainder is supplied by evaluating the asymptotes of the arctan function that fits the data. Considering the SAF in interferogram 26514, we base our estimates on samples within 60 m or more of the fault for narrowest width transition zones, and within 300 m for the widest that are encountered. For the mean width transition where $w = 22$ m, elastic dislocation theory would imply the approach of subsurface slip on a discrete dislocation to within 3–5 m of the surface of a half space. We discuss the consequences of this subsurface slip in a following section. Although our width estimates are spatially smoothed by our averaging algorithms, and therefore may represent much narrower zones, some ≈3-km-long segments of the fault clearly show >100-m-wide (w_{80}) shear zones. In these broader locations multiple surface fractures are evident, some at oblique angles to the strike of the main fault. The kinematic behavior of these short segments is probably controlled by local structures, minor transpressive or transtensive features along-strike, or variations in fault rheology in the uppermost several hundred meters of the fault.

From the LOS slip in Figures 5 and 7b we interpret the UAVSAR data as dextral slip s_D and compare it to triggered slip mapped during post-seismic fieldwork reported by Rymer et al. (2010) in Figure 9. Since the

radar views the scene from above, actual dextral slip may be larger or smaller if dip slip is present, although none was reported at sites mapped by Rymer et al. (2010) and although we assume in what follows that vertical offsets are negligible, we note that Wei et al. (2011) report maximum InSAR-inferred vertical motions locally approach one third of the maximum dextral motion. In Figure 9a we project the UAVSAR data as dextral slip together with triggered dextral slip mapped during post-seismic fieldwork following EMC (Rymer et al., 2010).

Several studies indicate that triggered slip on the southern SAF is confined to transpressional segments of the fault, each approximately 12.5 km long and separated by intervening right-stepping segments with strike closer to the plate boundary slip vector (Bilham & Williams, 1985; Lindsey et al., 2014; Williams et al., 1988). The UAVSAR data indicate that triggered slip in 2010 occurred not only on these transpressional segments but also within the intervening North Shore segment (Figure 9b). Lindsey et al. (2014) report a broad >200-m-wide shear zone in this segment. Our data show also that in addition to fault slip, off-fault deformation occurred over a wide region throughout the Mecca Hills and Durmid Hill, and that minor slip occurred also on the Hidden Springs fault to the north of the SAF. Triggered slip on the en-echelon strands of the Hidden Springs Fault is plausible in light of the many EMC-triggered slip segments of regional non-SAF faults documented previously (Rymer et al., 2010; Wei et al., 2011; Donnellan et al., 2014).

Triggered slip accompanies the passage of surface waves from distant earthquakes (Bilham & Castillo, 2020), and releases strain stored near the shallow fault imposed by plate boundary shear stresses. The incremental static strain induced by the EMC earthquake at Durmid Hill is insignificant compared to the fault zone shear strain responsible for creep rates in the valley (Table 2), although Xu et al. (2018) argue that it may influence subsequent slip rates on the fault. The rate of surface creep is governed by the ratio of the depth of surface slip to the depth of base of the seismogenic zone and the applied regional shear strain rate. Sieh and Williams (1990) inferred a depth for creep of 1.6 ± 0.6 km. Our finding that off-fault dextral triggered shear may equal that recorded as slip on the fault, would need this slip depth to be doubled, however, it is possible that non-triggered creep may be restricted to shallower depths.

3.2. Durmid and Mecca Hills Mapped Surface Slip Compared With UAVSAR Slip

Where surface mapping and UAVSAR data overlap, triggered dextral shear is underestimated by surface observations. In the Mecca Hills the mean UAVSAR-derived triggered slip in 2010 was 16.2 ± 5.9 mm and on Durmid Hill it amounted to 15.1 ± 3.7 mm. These are consistent with the maximum mapped slips of 18 and 15 mm respectively, but are 73% and 47% larger than the average observed surface offsets of 9.5 ± 4.6 mm and 7.1 ± 3.7 mm respectively. Since mapped slip reported in 2010 was similar in amplitude and spatial distribution to mapped slip triggered by previous nearby earthquakes, it follows that previous estimates of triggered slip were also underestimated.

A possible systematic bias for underestimating fault slip in field mapping follows from a unique observation in the 2004 Parkfield earthquake. Surface afterslip was undetectable at Work Ranch on the southern segment of the surface rupture until strain in the soils overlying the surface fault exceeded approximately 400 μstrain (Bilham, 2005). This was recorded by a creepmeter as subsurface extension gradually increasing over 3 days to 5 mm. It is thus probable that during triggered slip in 2010, shear displacements below 5 mm within the fault zone during triggered slip in 2010 left no visible evidence for surface offsets. Where they were visible, the 2010 offsets consisted of discontinuous en-echelon cracks following the fault zone, often curved and rarely parallel to the strike of the fault (Rymer et al., 2010). These are suggestive of shear strain rather than localized surface rupture.

Consistent with this inference is the observation that no surface offsets occurred on the surface fault above any of the creepmeters (Rymer et al., 2010) despite quantitative records for the timing of 3–4.8 mm subsurface extension across the fault zone at just 0.5 m depth (Figure 2a). In 2017 near creepmeter SC during a succeeding triggered slip episode, a distinct line of slip was observed at the base of a 3-m-deep gully that could not be followed to the surface (T. Rockwell, personal communication, 2021). The simplest interpretation of the absence of mappable surface slip is that surface strains were insufficient to crack surface soils, and that the signal measured by the creepmeters was not fault slip but fault zone shear strain. The maximum strain recorded by the southernmost creepmeter in 2010 was 343 μstrain (4.8 mm in 14 m).

Table 5
First Row Indicates Mean UAVSAR Observed Width and Dextral-Shear for the Durmid Segment of the SAF

Location	S_D (MM)	$Creep_{Obs}$(mm)	$Depth_{Calc}$(m)	$Width_{Calc}$ (m)	W_{80} (m)
$Durmid_{ave}$	15.1	4.8	13.4	80	134 ± 81
DU	8.0	4.8	6.3	38	51 ± 26
SC	12.9	3.7	15.0	90	52 ± 51
FE	18.7	3	27.4	164	165 ± 35

Note. The remaining three rows apply to creepmeter locations, and calculated surface locking depth and width for subsurface creep.

3.3. Near-Surface Fault Rheology and Changes in Surface Locking Depth 2004–2020

Hitherto creep in the Coachella valley has been assumed to extend from the surface to depths of the order of 1.6 km based on long term creep rates (Sieh & Williams, 1990), or ≈2.5 km from detailed studies of triggered slip (Tymofyeyeva et al., 2019). These studies characterize the depth of the transition from the locked seismogenic fault to the base of the creeping zone as the upper locking depth. We now introduce the notion of a surface locking depth, a depth below the surface above which the shallow fault is locked. The existence of a surface locking depth for creep on segments of Durmid Hill is implied by the absence of localized surface fault offsets, and the consequences of reconciling the numerical observations of antisymmetric shear strain (width and slip from UAVSAR), and observed strain (inferred from embedded creepmeters). Were the fault embedded in an elastic half space underlain by a planar dislocation we could solve for this locking depth. The elasto-plastic rheology of this surface layer is of interest since it moderates the surface expression of an active fault on which all paleoseismic trench studies are based.

The concept of a locked surface fault is an apparent contradiction. Clearly the surface fault does indeed slip during earthquakes. However, during the interseismic period, creep and triggered slip, which are considered to behave at depth as planar slip on a distinct fault surface penetrates through this surface layer as a distributed shear zone meters to tens of meters wide. The assumption of planar slip at shallow depth provides a starting point for interpreting the observed fault slip behavior 2004–2020.

To calculate local surface locking depths, we use UAVSAR observations of triggered shear width and dextral shear amplitude closest to each of the creepmeters (Table 5). For applied dextral shear of 8 mm and deformation width of 51 ± 26 m (the two closest UAVSAR observations) we determined analytically a surface locking depth of 6.3 m and shear zone width of 25 m (Figure 10). For a different time span Lindsey et al. (2014), Figure 5a calculate a fault zone shear width for this location of 110 ± 50 m implying an ≈18 m deep surface locking depth. Calculations at the other two creepmeter locations using local UAVSAR estimates for applied triggered shear and width yielded dislocation depths of 15 m at Salt Creek (SC) and 27 m at Ferrum (FE).

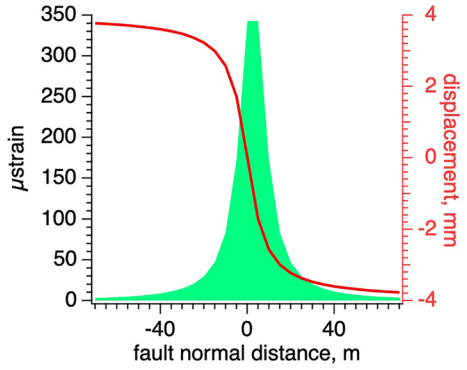

Figure 10. Antisymmetric fault zone displacements and creepmeter-measured strain as a function of distance from a creeping fault locked above 6.3 m depth subjected to 8 mm of applied shear (Table 1). 80% of the shear occurs within a 38 m wide zone (≈6 times the locking depth).

The result implies that the surface fault includes a tough carapace whose rheology can sustain shear strain but is resistant to throughgoing slip. This unexpected result resembles the behavior of shallow coseismic slip and afterslip on the West Napa fault described by Brooks et al. (2017). Brooks et al. (2017) found that >1 m of coseismic slip failed to rupture the surface but terminated at 3–25 m depth subjecting surface materials to distributed shear. Our inferred subsurface slip is two orders of magnitude less than theirs but the geometry appears to be similar.

The surface fault that we encountered while installing the creepmeters consists of a 3–5 m wide foliated gouge zone consisting of interleaved phacoidal clasts (Vannucchi, 2019) with dimensions of 2–20 cm. We propose that the ensemble response of these clasts is to act as a buffer to inhibit planar subsurface slip from surface expression as a linear break. We envisage that the surface fault severs a path through these clasts only in major earthquakes or in occasional creep-events. Thus, what has hitherto

been interpreted as interseismic creep on the surface above the fault is distributed strain caused by rearrangement and rotation of the clasts in the fault zone. In this scenario the creep-meters record strain, not fault offset.

We envisage that during subsurface slip, the foliated surface layer behaves as a continuum of interlocked materials obeying elastoplastic constitutive laws. Thus during subsurface slip the deformation of this surface layer closely resembles that of an elastic layer, but the imprinted elastic strain subsequently behaves as non-recoverable plastic strain, possibly through minor rotational adjustments of the foliated clasts. A characteristic arc-tan surface displacement field has been directly observed by Brooks et al. (2017, 2018) on creeping faults in northern California. Evidence for plastic deformation in the Mecca Hills is recorded as contiguous off-fault deformation in the form of curved drainages extending >800 m from the surface fault, absorbing as much as 10% of fault slip (Gray et al., 2018; Reitman et al., 2019). The transition from elastic surface deformation to plastic deformation progresses with time as demonstrated by the transition from strain to surface cracking in the days following the Parkfield earthquake (Bilham, 2005). A discontinuity in the elastic process occurs at the moment that the elasto-plastic limit is exceeded (surface cracks), which results in a change of surface boundary conditions. Our extensometer data confirm that during triggered slip, it is quite common for large strains (>300 μstrain) to be recorded within the surface fault without surface cracking. Clearly denser surface measurements would permit more complex behavior to be distinguished, but in their absence, we adopt the simplistic assumption that the observed arctan function is symptomatic of the response of surface elastic layer to slip below a distinct locking depth

A shallow slip-resistant layer accounts for the surface expression of creep on Durmid Hill during previous triggered episodes as discontinuous en-echelon cracks. A similar surface layer was reported by Scott et al. (2020) at Dry Creek. Rarely, slip is manifest on the southernmost SAF as an almost continuous line of surface cracking, as was triggered by the 2017 Chiapas earthquake (Tymofyeyeva et al., 2019, supplement S9). Occasional surface failure of the surface-resistant layer evidently occurs if we are to explain the apparently discrete offset of berms, channels, shorelines, concrete structures and rail lines (Blanton et al., 2020; Sieh & Williams, 1990). The fault-normal width of these long-term offsets varies from 8 cm to 2 m.

Brooks et al. (2017) observe that for the South Napa 2014 earthquake, the subsurface coseismic slip propagated to the surface as afterslip in the following days to weeks. This afterslip erased the coseismic surface slip deficit within about a month. In 2010 on Durmid Hill no afterslip occurred.

Our measurements address the important question of how effectively long-term dextral surface creep of the fault is characterized by measurements of discrete offsets of the surface fault and creep measurements, and whether these numerous fault observations can be corrected empirically to more accurately evaluate subsurface slip. One potential difficulty in addressing this issue is whether the broader deformation we observe during triggered slip is representative of deformation during slow aseismic slip between triggered events. Our proposed model is testable in that the width of the surface deformation zone provides a measure of the variable thickness of the rheological carapace that inhibits discrete surface slip. The width of the zone is approximately 6 times the thickness of this layer. However, given a creep rate of 2 mm/yr an empirical correction will only be quantifiable with UAVSAR measurements only after several years of measurement.

A larger earthquake hazard assessment issue arises if off-fault deformation is substantial during major earthquakes on the southern SAF. Studies of deformed and deflected drainages through the Mecca Hills reveal that long-term deformation is accommodated by non-recoverable plastic shear absorbed to distances of hundreds of meters from the surface fault (Gray et al., 2018). If this prevails it would render paleoseismic estimates of slip (derived from ≈10-m-wide trenches across the fault) lower than slip at depth (Reitman et al., 2019, as proposed by Grant and Donnellan (1994) from measurements of the SAF in the Carrizo Plain. Our current UAVSAR data provide a spatial foundation from which these effects may be quantified in a future earthquake.

4. Conclusions

We investigate the utility of UAVSAR remotely sensed repeat pass interferometry line of sight displacement maps for identifying and characterizing triggered fault slip on the southernmost San Andreas Fault and nearby faults, in the context of geological mapping, creepmeter data and GNSS records.

All pixels on recognized SAF and HSF traces detected by auto-edge detection methods are consistent with dextral shear. Slip is spatially discontinuous and has variable amplitude along strike. While we have not analyzed the pattern of slip and width on the HSF segments in detail, our preferred inference is triggered slip on the main Hidden Spring and Powerline faults, while the concentrated phase gradient on the Hot Springs fault may be due to deposited canal water impinging on an impermeable fault zone without ruling out possible triggered slip.

On the SAF, the width of triggered shear in some places is sufficiently narrow to be indistinguishable from discrete fault slip, but in many places, it exceeds 125 m and, in some segments, approaches 350 m. Regardless of shear-zone width, projected slip estimates are in the range 5–18 mm, with the caveat that values of slip s_R less than 5 mm are ignored since they are close to the noise level in the measurements. Corresponding inferred dextral slip average ≈15 mm with a high of 16.6 $\pm$ 6 mm in the Mecca Hills and a low of 13.7 $\pm$ 4 mm in a segment near North Shore where triggered slip has hitherto not been detected. Compared to geological mapping shortly after the 4/4/2010 EMC earthquake, the UAVSAR measurements indicate both more widespread along-strike slip, and a broader zone of deformation, including slip on numerous subsidiary features near the fault. We conclude that distributed shear may have been associated with previous episodes of triggered slip and not been recognized in these regions.

A surprising finding deduced from the combination of radar and creepmeter measurements on Durmid Hill is that creep and triggered slip are rarely expressed as discrete surface slip on a mapped fault. In 2010 triggered slip in the shallow subsurface was expressed as a zone of concentrated shear above the surface fault with a fault-normal width of 2–350 m. We introduce the concept of a "surface locking depth," above which the surface fault is locked during creep or triggered slip, to distinguish it from the "upper locking depth" at the base of the creeping fault which defines the top of the seismogenic zone. Triggered aseismic slip extends from the upper locking depth (>1 km) to the surface locking depth, within 4–6 m of the surface, above which slip is manifest as distributed surface shear. This barrier to surface slip is equated with a zone of phacoidal foliated gouge ubiquitous to the fault zone through Durmid Hill and the Mecca Hills. We speculate that internal rotation and translation of phacoidal clasts in this zone inhibits surface slip, transforming subsurface planar rupture into a zone of distributed surface shear. Deformation is distributed over a broad zone near the surface that in our current model takes the form of an arctangent function, whose fault-normal width is approximately six times its thickness.

Although the identification of a tough surface layer resistive to planar slip along the active trace of the San Andreas fault on Durmid Hill was unexpected, this rheology resembles that reported by Brooks et al. (2017) for the South Napa Fault. In order to account for the localized offset of channels, major earthquakes and large creep events in the Coachella Valley, must occasionally rupture through this surface shear zone. This has not occurred on Durmid Hill in the interval 2004–2020, but in 2017 may have occurred locally in the SE Mecca Hills (Tymofyeyeva et al., 2019).

Data Availability Statement

Creeepmeter data are archived at UNAVCO https://www.unavco.org/data/strain-seismic/creep-data/creep-data.html. GNSS time series are analyzed at JPL and in this work are accessed through the GeoGeogateway Science Portal (https://geo-gateway.org) Radar data for this research are available in the UAVSAR repository at the Alaska Satellite Facility, https://doi.org/10.5067/7PEQV8SVR4DM. The UAVSAR parsing and edge detection software used for this analysis can be accessed at https://github.com/GeoGateway/BuriedSAFSlip2010.

Acknowledgments
This work was carried out at the Jet Propulsion Laboratory, California Institute of Technology, under a contract with the National Aeronautics and Space Administration (80NM0018D0004). Operation of the creepmeters was funded by USGS 2004 to 2011 and in 2019 by NSF EAR 1941558.

References

Allen, C. R., Wyss, M., Brune, J. N., Granz, A., & Wallace, R. (1972). Displacements on the Imperial, Superstition Hills, and San Andreas faults triggered by the Borrego Mountain earthquake. In *U.S. Geological Survey Professional Paper*, *787*, 87–104. https://authors.library.caltech.edu/49795/1/Allen_1972p87.pdf

Behr, W. M., Rood, D. H., Fletcher, K. E., Guzman, N., Finkel, R., Hanks, T. C., et al. (2010). Uncertainties in slip-rate estimates for the Mission Creek strand of the southern San Andreas fault at Biskra Palms Oasis, southern California. *GSA Bulletin*, *122*(9–10), 1360–1377. https://doi.org/10.1130/b30020.1

Bilham, R. (2005). Coseismic strain and the transition to surface afterslip recorded by creepmeters near the 2004 Parkfield epicenter. *Seismological Research Letters*, *76*(1), 49–57. https://doi.org/10.1785/gssrl.76.1.49

Bilham, R., & Castillo, B. (2020). The July 2019 Ridgecrest, California, earthquake sequence recorded by creepmeters: Negligible epicentral afterslip and prolonged triggered slip at teleseismic distances. *Seismological Research Letters*, *91*(2A), 707–720. https://doi.org/10.1785/0220190293

Bilham, R., & Williams, P. (1985). Sawtooth segmentation and deformation processes on the southern San Andreas fault, California. *Geophysical Research Letters*, *12*(9), 557–560. https://doi.org/10.1029/gl012i009p00557

Blanton, C. M., Rockwell, T. K., Gontz, A., & Kelly, J. T. (2020). Refining the spatial and temporal signatures of creep and co-seismic slip along the southern San Andreas Fault using very high resolution UAS imagery and SfM-derived topography, Coachella Valley, California. *Geomorphology*, *357*, 107064. https://doi.org/10.1016/j.geomorph.2020.107064

Brooks, B. A., Liu, Z., Nevitt, J., Lundgren, P., Glennie, C. L., Page, M. T., et al. (2018). Shallow Fault Slip and Near-fault Deformation on the Creeping Section of the San Andreas Fault. *In AGU Fall Meeting Abstracts* (Vol. 2018, pp. T42D–06). https://ui.adsabs.harvard.edu/abs/2018AGUFM.T42D..06B/abstract

Brooks, B., Minson, S. E., Glennie, C. L., Nevitt, J. M., Dawson, T., Rubin, R., et al. (2017). Buried shallow fault slip from the South Napa earthquake revealed by near-field geodesy. *Science Advances*, *3*(7), e1700525. https://doi.org/10.1126/sciadv.1700525

Bryant, W. A. (1987). San Andreas and Hot Springs faults, northern imperial county, California: California Division of Mines and Geology Fault Evaluation FER-191 Report 191.

Bryant, W. A. (2012). San Andreas, Hidden Spring, Skeleton Canyon, Mecca Hills, and related faults, Riverside and Imperial Counties: California Geological Survey Fault Evaluation Report FER-252, 29 p.

Bryant, W. A. (2015). San Andreas, Skeleton Canyon, Indio Hills, NW Painted Canyon, Coachella Fan, Berdoo Canyon, and related faults, Riverside County, California Geological Survey Fault Evaluation Report FER-250.

Canny, J. (1986). A computational approach to edge detection. *IEEE Transactions on Pattern Analysis and Machine Intelligence*, *6*, 679–698. https://doi.org/10.1109/tpami.1986.4767851

Donnellan, A., Grant Ludwig, L., Parker, J. W., Rundle, J. B., Wang, J., Pierce, M., et al. (2015). Potential for a large earthquake near Los Angeles inferred from the 2014 La Habra earthquake. *Earth and Space Science*, *2*(9), 378–385. https://doi.org/10.1002/2015ea000113

Donnellan, A., Parker, J., Heflin, M., Glasscoe, M., Lyzenga, G., Pierce, M., et al. (2021). Improving access to geodetic imaging crustal deformation data using GeoGateway. *Earth Science Informatics*. https://doi.org/10.1007/s12145-020-00561-7

Donnellan, A., Parker, J., Heflin, M., Lyzenga, G., Moore, A., Ludwig, L. G., et al. (2018). fracture advancing step tectonics observed in the Yuha Desert and Ocotillo, CA, following the 2010 Mw7. 2 El Mayor-Cucapah Earthquake. *Earth and Space Science*, *5*(9), 456–472. https://doi.org/10.1029/2017ea000351

Donnellan, A., Parker, J., Hensley, S., Pierce, M., Wang, J., & Rundle, J. (2014). UAVSAR observations of triggered slip on the Imperial, Superstition Hills, and East Elmore Ranch Faults associated with the 2010 M 7.2 El Mayor-Cucapah earthquake. *Geochemistry, Geophysics, Geosystems*, *15*(3), 815–829. https://doi.org/10.1002/2013gc005120

Evans, E. L., Loveless, J. P., & Meade, B. J. (2015). Total variation regularization of geodetically and geologically constrained block models for the Western United States. *Geophysical Journal International*, *202*, 713–727. https://doi.org/10.1093/gji/ggv164

Evans, E. L., Thatcher, W. R., Pollitz, F. F., & Murray, J. R. (2016). Persistent slip rate discrepancies in the eastern California (USA) shear zone. *Geology*, *44*, 691–694. https://doi.org/10.1130/G37967.1

Fialko, Y. (2006). Interseismic strain accumulation and the earthquake potential on the southern San Andreas fault system. *Nature*, *441*(7096), 968–971. https://doi.org/10.1038/nature04797

Grant, L. B., & Donnellan, A. (1994). 1885 and 1991 surveys of the San Andreas fault: Implications for fault mechanics. *Bulletin Seismological Society of America*, *84*, 241–246. https://www.seismosoc.org/publications/bssa/

Gray, H. J., Shobe, C. M., Hobley, D. E., Tucker, G. E., Duvall, A. R., Harbert, S. A., & Owen, L. A. (2018). Off-fault deformation rate along the southern San Andreas fault at Mecca Hills, southern California, inferred from landscape modeling of curved drainages. *Geology*, *46*(1), 59–62. https://doi.org/10.1130/g39820.1

Hays, W. H. (1957). *Geology of the Central Mecca Hills, Riverside County, California*. Yale University unpublished Ph.D. thesis.

Heflin, M., Donnellan, A., Parker, J., Lyzenga, G., Moore, A., Ludwig, L. G., et al. (2020). Automated estimation and tools to extract positions, velocities, breaks, and seasonal terms from daily GNSS measurements: Illuminating nonlinear Salton Trough deformation. *Earth and Space Science*, *7*(7), e2019EA000644. https://doi.org/10.1029/2019ea000644

Hensley, S., Wheeler, K., Sadowy, G., Jones, C., Shaffer, S., Zebker, H., et al. (2008). The UAVSAR instrument: Description and first results. In *2008 IEEE Radar Conference*. (pp. 1–6). IEEE. https://www.researchgate.net/profile/Kevin-Wheeler-4/publication/224361281_The_UAVSAR_instrument_Description_and_first_results/links/56250c5308ae4d9e5c4b9c35/The-UAVSAR-instrument-Description-and-first-results.pdf

Hensley, S., Zebker, H., Jones, C., Michel, T., Muellerschoen, R., & Chapman, B. (2009). First deformation results using the NASA/JPL UAVSAR instrument. In *2009 2nd Asian-Pacific conference on synthetic aperture radar*. (pp. 1051–1055). IEEE. https://ieeexplore.ieee.org/document/5374246

Jänecke, S. U., Markowski, D. K., Evans, J. P., Persaud, P., & Kenney, M. (2018). Durmid ladder structure and its implications for the nucleation sites of the next M>7.5 earthquake on the San Andreas fault or Brawley seismic zone in southern California. *Lithosphere*, *10*(5), 602–631. https://doi.org/10.1130/l629.1

Jennings, C. W., & Bryant, W. A. (2010). *Fault Activity Map of California Geologic Data Map Number 6*. California Geological Survey. https://www.conservation.ca.gov/cgs/publications/fault-activity-map-of-california

Jones, L. M., Bernknopf, R. L., Cox, D. A., Goltz, J., Hudnut, K. W., Mileti, D. S., et al. (2008). *The ShakeOut Scenario: Effects of a potential M7.8 earthquake on the San Andreas fault in Southern California*. US Geological Survey. https://pubs.usgs.gov/of/2008/1150/

Lindsey, E. O., Fialko, Y., Bock, Y., Sandwell, D. T., & Bilham, R. (2014). Localized and distributed creep along the southern San Andreas Fault. *Journal of Geophysical Research: Solid Earth*, *119*(10), 7909–7922. https://doi.org/10.1002/2014jb011275

Lundgren, P., Hetland, E. A., Liu, Z., & Fielding, E. J. (2009). Southern San Andreas-San Jacinto fault system slip rates estimated from earthquake cycle models constrained by GPS and interferometric synthetic aperture radar observations. *Journal of Geophysical Research: Solid Earth*, *114*(B2). https://doi.org/10.1029/2008jb005996

Lyons, S., & Sandwell, D. (2003). Fault creep along the southern San Andreas from interferometric synthetic aperture radar, permanent scatterers, and stacking. *Journal of Geophysical Research: Solid Earth*, *108*(B1). https://doi.org/10.1029/2002jb001831

Manzo, M., Fialko, Y., Casu, F., Pepe, A., & Lanari, R. (2012). A quantitative assessment of DInSAR measurements of interseismic deformation: The Southern San Andreas Fault case study. *Pure and Applied Geophysics*, *169*(8), 1463–1482. https://doi.org/10.1007/s00024-011-0403-2

McNabb, J. C., Dorsey, R. J., Housen, B. A., Dimitroff, C. W., & Messe, G. T. (2017). Stratigraphic record of Pliocene-Pleistocene basin evolution and deformation within the southern San Andreas fault zone, Mecca Hills, California. *Tectonophysics*, *719*, 66–85. https://doi.org/10.1016/j.tecto.2017.03.021

Parker, J., Glasscoe, M., Donnellan, A., Stough, T., Pierce, M., & Wang, J. (2018). Radar determination of fault slip and location in partially decorrelated images. In *Earthquakes and Multi-Hazards Around the Pacific Rim* (Vol. I, pp. 101–116). Birkhäuser. https://doi.org/10.1007/978-3-319-71565-0_8

Philibosian, B., Fumal, T., & Weldon, R. (2011). San Andreas fault earthquake chronology and Lake Cahuilla history at Coachella, California. *Bulletin of the Seismological Society of America*, *101*(1), 13–38. https://doi.org/10.1785/0120100050

Platt, J. (2017). Persistent slip rate discrepancies in the eastern California (USA) shear zone: Comment. *Geology*, *45*(9), e425. https://doi.org/10.1130/g39345c.1

Reitman, N. G., Mueller, K. J., Tucker, G. E., Gold, R. D., Briggs, R. W., & Barnhart, K. R. (2019). Offset channels may not accurately record strike-slip fault displacement: Evidence from landscape evolution models. *Journal of Geophysical Research: Solid Earth*, *124*(12), 13427–13451. https://doi.org/10.1029/2019jb018596

Riemann, R. A., Evans, J. P., Jänecke, S. U., Donnellan, A., & Parker, J. (2020). Using creep-related features and geodetic analyses to define the location, slip rate, and geometry of off-fault deformation, Hidden Spring fault zone, southern California: Geological Society of America Abstracts with Programs. (Vol. 52, No. 3). https://digitalcommons.usu.edu/cgi/viewcontent.cgi?article=1625&context=spacegrant

Rockwell, T. K., Meltzner, A. J., & Haaker, E. C. (2018). Dates of the Two most recent surface ruptures on the Southernmost San Andreas fault recalculated by precise dating of lake Cahuilla dry periods. *Bulletin of the Seismological Society of America*, *108*(5A), 2634–2649. https://doi.org/10.1785/0120170392

Rymer, M. J., Treiman, J. A., Kendrick, K. J., Lienkaemper, J. J., Weldon, R. J., Bilham, R., et al. (2010). *Triggered surface slips in southern California associated with the 2010 El Mayor-Cucapah, Baja California, Mexico, earthquake*. (p. 1333). US Geological Survey Open-File Report. https://pubs.usgs.gov/of/2010/1333/of2010-1333_ebook.pdf

Savage, J. C., & Prescott, W. H. (1978). Asthenosphere readjustment and the earthquake cycle. *Journal of Geophysical Research: Solid Earth*, *83*(B7), 3369–3376. https://doi.org/10.1029/jb083ib07p03369

Scott, C., Bunds, M., Shirzaei, M., & Toke, N. (2020). Creep along the Central San Andreas Fault from surface fractures, topographic differencing, and InSAR. *Journal of Geophysical Research: Solid Earth*, *125*, e2020JB019762. https://doi.org/10.1029/2020JB019762

Sieh, K. E. (1986). Slip rate across the San Andreas fault and prehistoric earthquakes at Indio, California. *Eos, Transactions American Geophysical Union*, *67*(44), 1200. https://agupubs.onlinelibrary.wiley.com/journal/23249250

Sieh, K. E., & Williams, P. L. (1990). Behavior of the southernmost San Andreas fault during the past 300 years. *Journal of Geophysical Research: Solid Earth*, *95*(B5), 6629–6645. https://doi.org/10.1029/jb095ib05p06629

Sylvester, A. G., Bilham, R., Jackson, M., & Barrientos, S. (1993). Aseismic growth of Durmid Hill, southeasternmost San Andreas fault, California. *Journal of Geophysical Research: Solid Earth*, *98*(B8), 14233–14243. https://doi.org/10.1029/93jb01028

Thomann, C., Jänecke, S. U., Evans, J. P., Markowski, D., Quinn, R., & Quinn, R. (2019). Could a Keystone Fault Block Explain the Overdue Timing of a M 7.5+ earthquake Along The Southern San Andreas Fault? (Vol. 51(5)). Geological Society of America Abstracts with Programs. https://doi.org/10.1130/abs/2019AM-332595

Tong, X., Smith-Konter, B., & Sandwell, D. T. (2014). Is there a discrepancy between geological and geodetic slip rates along the San Andreas Fault System? *Journal of Geophysical Research: Solid Earth*, *119*(3), 2518–2538. https://doi.org/10.1002/2013jb010765

Tymofyeyeva, E., Fialko, Y., Jiang, J., Xu, X., Sandwell, D., Bilham, R., et al. (2019). Slow slip event on the Southern San Andreas fault triggered by the 2017 M w 8.2 Chiapas (Mexico) earthquake. *Journal of Geophysical Research: Solid Earth*, *124*(9), 9956–9975. https://doi.org/10.1029/2018jb016765

U S Geological Survey and California Geological Survey. (2020). Quaternary fault and fold database for the United States. https://www.usgs.gov/natural-hazards/earthquake-hazards/faults

Van der Woerd, J., Klinger, Y., Sieh, K., Tapponnier, P., Ryerson, F. J., & Mériaux, A. S. (2006). Long-term slip rate of the southern San Andreas fault from 10Be-26Al surface exposure dating of an offset alluvial fan. *Journal of Geophysical Research: Solid Earth*, *111*(B4). https://doi.org/10.1029/2004jb003559

Vannucchi, P. (2019). Scaly fabric and slip within fault zones. *Geosphere*, *15*(2), 342–356. https://doi.org/10.1130/ges01651.1

Wei, M., Sandwell, D., Fialko, Y., & Bilham, R. (2011). Slip on faults in the Imperial Valley triggered by the 4 April 2010 Mw 7.2 El Mayor-Cucapah earthquake revealed by InSAR. *Geophysical Research Letters*, *38*(1). https://doi.org/10.1029/2010gl045235

Williams, P. L., McGill, S. F., Sieh, K. E., Allen, C. R., & Louie, J. N. (1988). Triggered slip along the San Andreas fault after the 8 July 1986 North Palm Springs earthquake. *Bulletin of the Seismological Society of America*, *78*(3), 1112–1122. https://doi.org/10.1785/bssa0780031112

Xu, X., Ward, L. A., Jiang, J., Smith-Konter, B., Tymofyeyeva, E., Lindsey, E. O., et al. (2018). Surface creep rate of the southern San Andreas fault modulated by stress perturbations from nearby large events. *Geophysical Research Letters*, *45*(19), 10–259. https://doi.org/10.1029/2018gl080137